

# Discrete Elasto-Plastic Rods

Xuanhe Li<sup>1</sup>, Weicheng Huang<sup>1</sup>, M. Khalid Jawed<sup>\*</sup>

Department of Mechanical and Aerospace Engineering, University of California, Los Angeles, CA 90095, United States

## ARTICLE INFO

### Article history:

Received 11 February 2020

Received in revised form 22 April 2020

Accepted 10 May 2020

Available online 12 May 2020

### Keywords:

Rods  
Plasticity  
Numerical simulation

## ABSTRACT

We report a discrete differential geometry-based numerical framework to simulate the rate-independent, elasto-plastic behavior of one dimensional rod-like structures. Our numerical tool first discretizes the rod centerline into a number of nodes and edges in a manner similar to the well-established Discrete Elastic Rods (DER) method – a fast geometrically exact simulation for elastic filaments. The cross section of each vertex is next meshed into multiple fiber-like elements, such that the nonlinear constitutive relation of each element can be individually described by an increment-based associated flow rule and updated through return mapping algorithm. Equations of motion numerically obtained from energy variation at each degree of freedom are integrated through an implicit Euler time marching scheme, for its unconditional convergence and numerical stability. For quantitative comparison, we derive the analytical solutions for several simple cases, and a good match between the analytical solution and the numerical results in the geometrically linear regime indicates the accuracy of our discrete model. Our simulation can seamlessly handle the nonlinearity from both geometric and material sides, which is often not amenable to an analytical approach.

© 2020 Elsevier Ltd. All rights reserved.

## 1. Introduction

Rods are structures with length much larger than the width and thickness. Due to the slenderness of the geometry, this class of structures often undergo geometrically nonlinear deformation, as manifested in both natural (e.g. bacterial flagella) [1] and engineering (ropes, cables, and pipelines) [2] systems. The recent trend of exploiting large deformation in slender structures to design and fabricate metamaterials [3] indicates the need for computationally efficient simulation tools for slender structures. While an extensive amount of work has been done in modeling purely elastic rods in both mechanics [4] and computer graphics [5] communities, computational tools for rods with nonlinear constitutive relations, e.g. hyperelasticity [6], rate-dependent viscoelasticity [7,8], and elasto-plasticity [9], are relatively scarce. A commonly used nonlinear constitutive relation is elasto-plasticity that manifests itself in both simple materials [10–13] and advanced structures [14–16]. In this paper, we focus on modeling the elasto-plastic behavior in rod-like structures.

The first scholarly work on plasticity dates back to at least 1868, when Tresca [17] proposed an assumption that metals would flow when shear stress exceeds a threshold on basis of experimental observation. In rod-like structures, the deformation

can be decomposed into three components – bending, twisting, and stretching. The latter mode is negligible since geometric slenderness makes stretching energetically expensive. However, bending and twisting often appear simultaneously to pose a coupled problem. Prior works on elasto-plastic deformation of rods typically consider only bending [18,19] or twisting [20–22]. The few studies that consider combined bending and torsion restricted themselves to simplified material behavior, e.g. rigid-plastic [23–28], elastic-perfectly plastic [29–31], and Ramberg–Osgood stress–strain law [32]. This motivates us to develop a simulation algorithm for elasto-plastic rods that can account for combined bending, twisting, and stretching for an infinite number of loading and unloading cycles.

With the development of computational capability in the past few decades, Finite Element Method (FEM) [33–36] has become the preferred means for researchers and engineers in structural analysis involving elasto-plasticity. However, 3D simulations of slender rods undergoing bending and torsion with elasto-plastic constitutive law typically require volumetric mesh of small size. This can lead to computationally expensive simulations, especially when combining the nonlinearity from both geometric and material side. Recently, another type of numerical tools – Discrete Differential Geometry (DDG)-based methods [37] – are becoming increasingly popular in the computer graphics community for the simulation of thin elastic structures, e.g. hair and clothes, due to computational efficiency and robustness in handling geometric nonlinearity. The DDG-based approach starts with discretization of the smooth structure into a mass–spring-type system, while preserving the key geometric properties of

<sup>\*</sup> Corresponding author.

E-mail address: [khalidjm@seas.ucla.edu](mailto:khalidjm@seas.ucla.edu) (M.K. Jawed).

<sup>1</sup> X.L. and W.H. contributed equally to this work.

actual physical objects [37]. Previous DDG-based methods have shown surprisingly successful performance in simulating slender structures, e.g. rods [5,38–41], ribbons [42], plates/shells [43–45], and gridshells [46]. On the other hand, previous DDG-based numerical frameworks of filamentary rods usually assume that the structure is in linear elastic regime. Even though a more general model – rate-dependent viscoelastic constitutive law – has been considered in a recent study [7], it cannot be directly used for the investigation of elasto-plastic behavior of rods. Elasto-plasticity requires discretization of rod cross section such that the boundary between the elastic and the plastic regimes can be tracked.

Here, we propose a numerical method – Discrete Elasto-Plastic Rods (DEPR) – that combines a geometrically nonlinear description of a rod following Discrete Elastic Rods (DER) [5,38] method, with an increment-based plasticity flow model [9] to simulate the elasto-plastic behavior of rod-like structures during large deflection. DER is based on the classical Kirchhoff rod model. The rod centerline is first discretized into a number of nodes and the cross-section of each node is later divided into multiple fiber-like elements. The kinematics of the centerline is formulated in a manner similar to the DER method and the strain tensor at any point in the solid body is assumed to be a function of the deformation (bending, twisting, stretching) of the centerline. Next, an implicit returning mapping algorithm is used to update the stress tensor of each element on the basis of the increment of strain tensor – computed from the deformation of the rod centerline – together with its current von Mises equivalent stress [47,48]; The internal force vector, required by the equations of motion of rod system, is then computed from the increment of strain energies. In parallel with numerical investigation, we analytically obtain the force–displacement relations for some simple cases to quantitatively check the accuracy of our simulator. A good match between numerical simulation and analytical results in the linear phase indicates the correctness of the numerical scheme. While the analytical solutions do not hold for geometrically nonlinear deformation, the DDG-based simulation can robustly capture the nonlinearity from both geometric and material sides. Nonetheless, if the rod is undergoing pure bending (i.e. a beam) or torsion, several analytical and numerical methods discussed earlier in this section should be preferred due to low computational cost. DEPR is particularly useful when the slender rod is undergoing combined bending and twisting with repeated loading and unloading.

Our paper is organized as follows. In Section 2, we discuss the proposed DEPR simulator. Next, in Section 3, we conduct both numerical data and analytical results for several demonstrative examples. Finally, conclusive remarks and potential research avenues are presented in Section 4.

## 2. Methods

In this section, we introduce the numerical framework for simulating the mechanical response of elasto-plastic rods. We first discuss the kinematics of one dimensional rod-like structures in a discrete format, followed by a general rate-independent, increment-based nonlinear constitutive relation. Finally, we present the time marching scheme and the return mapping algorithm used in our simulator.

### 2.1. Discrete kinematics of rod

As shown schematically in Fig. 1(a), we discretize the centerline of a one dimensional rod-like structure into  $N$  nodes,  $[\mathbf{x}_0, \mathbf{x}_1, \dots, \mathbf{x}_{N-1}]$ , which correspond to  $N - 1$  edge vectors,  $[\mathbf{e}^0, \mathbf{e}^1, \dots, \mathbf{e}^{N-2}]$ . We use subscripts to denote quantities associated with the nodes, e.g.  $\mathbf{x}_i$ , and superscripts when associated

with edges, e.g.  $\mathbf{e}^i$ . Each edge,  $\mathbf{e}^i$ , has an orthonormal adapted reference frame  $\{\mathbf{d}_1^i, \mathbf{d}_2^i, \mathbf{t}^i\}$  and a material frame  $\{\mathbf{m}_1^i, \mathbf{m}_2^i, \mathbf{t}^i\}$ ; both the frames share the tangent  $\mathbf{t}^i = \mathbf{e}^i / \|\mathbf{e}^i\|$  as one of the directors [5,38]. The scalar twist angle,  $\theta^i$ , on an edge  $\mathbf{e}^i$  is the angle from  $\mathbf{d}_1^i$  to  $\mathbf{m}_1^i$  about the tangent  $\mathbf{t}^i$  (see Fig. 1(b)). An intriguing feature of DER is the choice of reference frame. During the time marching scheme (Section 2.3), the reference frame on each edge at time  $t = t_{n+1}$  (the  $(n + 1)$ th time step) is parallel transported from the reference frame at  $t = t_n$  (the  $n$ th time step). Parallel transport [38] is a method of moving  $\mathbf{d}_1^i(t_n)$  (perpendicular to tangent  $\mathbf{t}^i(t_n)$ ), without any tangential angular velocity (i.e. rotation about the tangent), to get  $\mathbf{d}_1^i(t_{n+1})$  that remains perpendicular to tangent  $\mathbf{t}^i(t_{n+1})$ . Positions of  $N$  nodes (corresponding to  $3N$  degrees of freedom) together with the twist angle at  $N - 1$  edges constitute the  $4N - 1$  sized degrees of freedom (DOF) vector,  $\mathbf{q} = [\mathbf{x}_0, \theta^0, \mathbf{x}_1, \dots, \mathbf{x}_{N-2}, \theta^{N-2}, \mathbf{x}_{N-1}]$ , of the discrete rod centerline [40,49].

The deformation of a rod centerline at the  $i$ th node can be decomposed into three types of strains: uniaxial stretching ( $\epsilon_i^u$ ), bending curvatures ( $\kappa_i^1, \kappa_i^2$ ), and twist ( $\tau_i$ ). We next discretize the rod circular cross section into  $M$  rectangular elements. For the  $j$ th element at the  $i$ th node in Fig. 1(b), we construct its center coordinates  $[X^{(i,j)}, Y^{(i,j)}]$  on the basis of its material frame,  $\{\mathbf{m}_1^i, \mathbf{m}_2^i, \mathbf{t}^i\}$ , and denotes its area as  $\Delta S^{(i,j)}$ . Note that the material frame is an edge-based quantity while our strains are calculated at the nodes. Therefore, we use the average of the material directors at the  $(i - 1)$ th edge and the  $i$ th edge as the node-based material directors, e.g. the first material director at the  $i$ th edge is  $(\mathbf{m}_1^{i-1} + \mathbf{m}_1^i)/2$ . Moreover, uniaxial stretching is conventionally used as an edge-based quantity [38]. In our case, we define this stretching as  $\epsilon_i^u = (\Delta l_i - \bar{\Delta} l_i) / \bar{\Delta} l_i$ , where  $\Delta l_i = (\|\mathbf{e}^{i-1}\| + \|\mathbf{e}^i\|)/2$  is the Voronoi length of the  $i$ th node,  $\|\mathbf{e}^i\|$  is the undeformed length of the  $i$ th edge, and  $\bar{\Delta} l_i$  is the Voronoi length in undeformed state. Based on the kinematics of Kirchhoff rod model, the strain tensor at the  $j$ th element of the  $i$ th node is given by

$$\epsilon^{(i,j)} = \begin{bmatrix} \epsilon_{11} & \epsilon_{12} & \epsilon_{13} \\ \epsilon_{21} & \epsilon_{22} & \epsilon_{23} \\ \epsilon_{31} & \epsilon_{32} & \epsilon_{33} \end{bmatrix} \quad (1)$$

where  $\epsilon_{12} = \epsilon_{21} = 0$ ,  $\epsilon_{13} = \epsilon_{31} = -\frac{1}{2}\tau_i Y^{(i,j)}$ ,  $\epsilon_{23} = \epsilon_{32} = \frac{1}{2}\tau_i X^{(i,j)}$ ,  $\epsilon_{33} = \epsilon_i^u + \kappa_i^2 X^{(i,j)} + \kappa_i^1 Y^{(i,j)}$ , and  $\epsilon_{11} = \epsilon_{22} = -\nu \epsilon_{33}$ , and  $\nu$  is the Poisson ratio. Here, we ignored the effect of warping. The expressions for  $\epsilon_i^u$ ,  $\kappa_i^1$ ,  $\kappa_i^2$ , and  $\tau_i$  in terms of the DOFs of the rod can be found in Refs. [38,40].

### 2.2. Constitutive laws

With the strain discussed above, we next formulate the elasto-plastic constitutive relation by an increment flow plasticity theory. We consider a plastic flow model with isotropic hardening, as shown in Fig. 1(c), when the von Mises stress at an element,  $\sigma_{eq}$ , goes beyond the threshold of the material,  $\sigma_{eq,c}$  (i.e.  $\sigma_{eq} > \sigma_{eq,c}$ ), the material is in the plastic domain and its modulus switches from  $E$  to  $E_t = EH/(E + H)$ . Here,  $E$  is the Young's modulus of material,  $H$  is its hardening modulus, and the von Mises stress is defined as

$$\sigma_{eq}(\sigma) = \left\{ \frac{1}{2} \left[ (\sigma_{11} - \sigma_{22})^2 + (\sigma_{22} - \sigma_{33})^2 + (\sigma_{33} - \sigma_{11})^2 + 6(\sigma_{23}^2 + \sigma_{31}^2 + \sigma_{12}^2) \right] \right\}^{1/2}. \quad (2)$$

In the current study, we use the plastic flow rule described in Ref. [9]. The relation between the increment of stress tensor  $\delta\sigma$  and strain tensor  $\delta\epsilon$  is given by

$$\delta\epsilon = \delta\epsilon_e + \delta\epsilon_p \quad (3a)$$

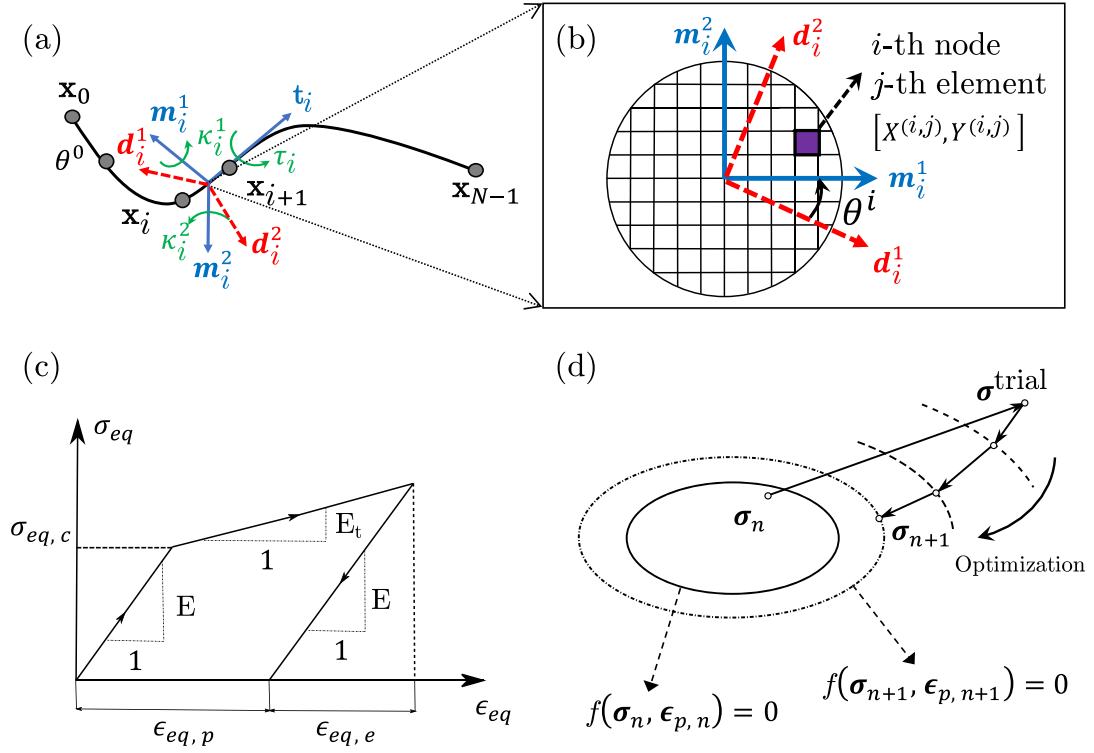


**Fig. 1.** (a) Schematic and relevant notations used in our discrete model. (b) Mesh of cross section. (c) Nonlinear constitutive relation. (d) Illustration of return-mapping algorithm.

$$\delta \epsilon_e = \mathbb{D}^{-1} : \delta \sigma \quad (3b)$$

$$\delta \epsilon_p = d\lambda \frac{\partial f}{\partial \sigma} \quad (3c)$$

where  $\mathbb{D}$  is the elastic stiffness tensor,  $\delta \epsilon_e$  is the increment of elastic strain,  $\delta \epsilon_p$  is the increment of plastic strain,  $d\lambda$  is the hardening parameter, and  $f$  is a criterion function defined by the outer surface of stress space,

$$f(\sigma, \epsilon_p) = \sigma_{ep}(\sigma) - \sigma_{eq,c} - H\epsilon_{eq}(\epsilon_p), \quad (4)$$

where  $\epsilon_{eq}(\epsilon_p)$  is the equivalent plastic strain and can be computed using Eq. (2) upon replacing the stress quantities with strain quantities. This criterion implies that the real stress should not go beyond the surface defined above,  $f(\sigma, \epsilon_p) \leq 0$ . Also, the associated flow rule indicates that the increment of the plastic strain should always be normal to the criterion function surface,  $\partial f / \partial \sigma$ . Note that Eq. (3b) can be written using the Voigt notation as

$$\begin{bmatrix} \delta \epsilon_{e,11} \\ \delta \epsilon_{e,22} \\ \delta \epsilon_{e,33} \\ \delta \epsilon_{e,23} \\ \delta \epsilon_{e,31} \\ \delta \epsilon_{e,12} \end{bmatrix} = \mathbf{S} \begin{bmatrix} \delta \sigma_{11} \\ \delta \sigma_{22} \\ \delta \sigma_{33} \\ \delta \sigma_{23} \\ \delta \sigma_{31} \\ \delta \sigma_{12} \end{bmatrix}, \quad (5)$$

where

$$\mathbf{S} = \frac{1}{E} \begin{bmatrix} 1 & -\nu & -\nu \\ -\nu & 1 & -\nu \\ -\nu & -\nu & 1 \\ & & & 2(1+\nu) \\ & & & & 2(1+\nu) \\ & & & & & 2(1+\nu) \end{bmatrix}. \quad (6)$$

### 2.3. Time marching scheme

At  $n$ th time step,  $t_n$ , we know the DOF vector  $\mathbf{q}_n$ , its velocity  $\mathbf{v}_n$ , stress tensor  $\sigma_n^{(i,j)}$ , and strain tensor  $\epsilon_n^{(i,j)}$ ; we need to solve

the equations of motion and update all the quantities from time  $t = t_n$  to  $t = t_{n+1} + h$  ( $h$  is the time step size) on the basis of the statement of force equilibrium; see Appendix A for an algorithm of the time marching scheme. The equations of motion for the  $4N - 1$  sized discrete rod system is [49]

$$\mathbf{E}_{n+1} \equiv \mathbf{M} \delta \mathbf{q}_{n+1} - h \mathbf{M} \mathbf{v}_n - h^2 (\mathbf{F}_{n+1}^{\text{int}} + \mathbf{F}_{n+1}^{\text{ext}}) = \mathbf{0} \quad (7a)$$

$$\mathbf{q}_{n+1} = \mathbf{q}_n + \delta \mathbf{q}_{n+1} \quad (7b)$$

$$\mathbf{v}_{n+1} = \frac{1}{h} \delta \mathbf{q}_{n+1}, \quad (7c)$$

where  $\mathbf{F}^{\text{int}}$  is the internal force vector (e.g. sum of stretching, bending and twisting forces),  $\mathbf{F}^{\text{ext}}$  is the external force vector (e.g. gravity and damping force),  $\mathbf{M}$  is the diagonal mass matrix comprised of the lumped masses, and, hereafter, superscript  $n+1$  (and  $n$ ) denotes evaluation of the quantity at time  $t_{n+1}$  (and  $t_n$ ). The internal force is derived by the increment of total strain energy,

$$\mathbf{F}^{\text{int}} = - \frac{\delta U}{\delta \mathbf{q}}, \quad (8)$$

where  $\delta U$  is given by

$$\delta U = \iiint (\sigma : \delta \epsilon) dV \quad (9a)$$

$$= \sum_{i=0}^{N-1} \left\{ \sum_{j=0}^{M-1} [\sigma^{(i,j)} : \delta \epsilon^{(i,j)} \Delta S^{(i,j)}] \Delta l_i \right\}. \quad (9b)$$

Note that without considering plastic deformation, the increment of strain energy can be simplified as

$$\delta U = \sum_{i=0}^{N-1} [EA \epsilon_i^u \delta \epsilon_i^u + EI (\kappa_i^1 \delta \kappa_i^1 + \kappa_i^2 \delta \kappa_i^2) + GJ \tau_i \delta \tau_i], \quad (10)$$

where  $I$  is the second moment of inertia of cross section, and  $J$  is its polar moment of inertia. In this case, discretization of

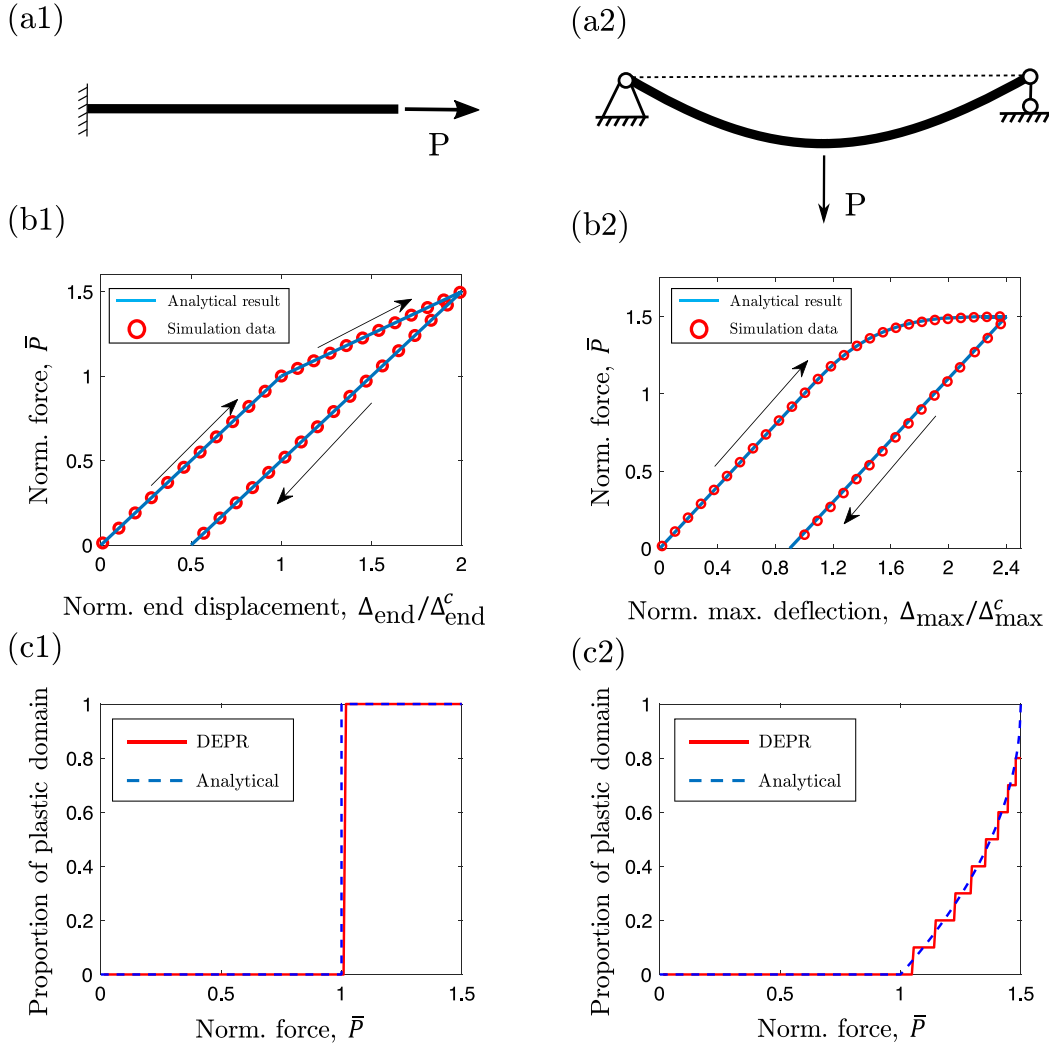


**Fig. 2.** Diagram of boundary and load conditions for (a1) uniaxial stretching and (a2) simply supported beam. Normalized force-displacement curve in one loading-unloading cycle for (b1) uniaxial stretching and (b2) simply supported beam. Evolution of plastic domain for (c1) uniaxial stretching and (c2) simply supported beam. When the portion of plastic domain is 1, all the elements through the cross-section has experienced yielding.

the cross-section into  $M$  fibers is not necessary and our method reduces to the DER method. On the other hand, there is no general analytical formulation for strain energy in nonlinear phase, such that the internal force and related strain energy can only be numerically computed from Eq. (9). Appendix B provides details on computation of the internal force.

With a prescribed increment of DOF vector,  $\delta \mathbf{q}_{n+1}$ , the increment of strain tensor on the  $(i, j)$ th element,  $\delta \epsilon_{n+1}^{(i,j)}$ , can be derived from Eq. (1); next, the increment of stress tensor should satisfy the following equations on the basis of constitutive law,

$$f(\sigma_{n+1}, \epsilon_{p,n+1}) = 0 \quad (11a)$$

$$\delta \sigma_{n+1} - \mathbb{D} : \left[ \delta \epsilon_{n+1} - d\lambda \frac{\partial f(\sigma_{n+1}, \epsilon_{p,n+1})}{\partial \sigma_{n+1}} \right] = 0, \quad (11b)$$

where  $\epsilon_{p,n+1} = \epsilon_{p,n} + \delta \epsilon_{p,n+1}$  and  $\sigma_{n+1} = \sigma_n + \delta \sigma_{n+1}$ . Here, we ignore the superscript  $(i, j)$  for simplification. Referring to Fig. 1(d), the implicit return mapping algorithm is used to iteratively solve the increment of stress tensor,  $\delta \sigma_{n+1}$ , as well as the hardening parameter,  $d\lambda$ , based on the prescribed strain increment,  $\delta \epsilon_{n+1}$ , and the current stress state,  $\sigma_n$ . See Appendix C for details on this algorithm. Once the new stress tensor is obtained, the total strain

energy and its gradient (i.e. negative value of the internal force) can be numerically derived from Eqs. (9) and (8).

The Jacobian associated with Eq. (7a) necessary for Newton's iteration can be expressed as

$$\mathbf{J} = \mathbf{M} - h^2 \left( \frac{\delta \mathbf{F}^{\text{int}}}{\delta \mathbf{q}} + \frac{\delta \mathbf{F}^{\text{ext}}}{\delta \mathbf{q}} \right), \quad (12)$$

and the Hessian matrix of strain energy,  $\delta \mathbf{F}^{\text{int}}/\delta \mathbf{q}$ , is numerically evaluated in a manner similar to the formulation of internal force; see Appendix B. Once the statement of force balance in Eq. (7a) is within the tolerance (i.e. computing  $\delta \mathbf{q}_{n+1}$ ), we update all the information, i.e.  $\mathbf{q}_{n+1}$  from Eq. (7b),  $\mathbf{v}_{n+1}$  from Eq. (7c),  $\epsilon_{n+1}^{(i,j)}$  from Eq. (1), and  $\sigma_{n+1}^{(i,j)}$  from Eq. (11), and move forward to the next time step.

### 3. Results

In this section, we use several examples in increasing complexity to demonstrate our newly introduced increment-based discrete elasto-plastic rod model; also, analytical solutions are derived for some simple cases to show the accuracy of our numerical framework. Appendix D shows the convergence of the

algorithm with the number of nodes and elements, using the second example discussed in this section.

### 3.1. Uniaxial stretching of a rod

We first consider a straight rod under uniaxial stretching shown schematically in Fig. 2(a1). Here, the geometric and physical parameters are: rod length  $L = 1.0\text{m}$ , radius of circular cross section  $r_0 = 1\text{mm}$ , Young's modulus  $E = 10\text{ GPa}$ , tangent modulus  $E_t = 5\text{ GPa}$ , Poisson's ratio is  $\nu = 0.3$ , and critical yield stress  $\sigma_{eq,c} = 10\text{ MPa}$ . The maximum uniaxial strain is less than 1%. We discretize the one dimensional rod into  $N = 20$  nodes and  $M = 80$  elements at each vertex.

In Fig. 2(b1), we plot the normalized tip displacement,  $\Delta_{\text{end}}/\Delta_{\text{end}}^c$ , versus the normalized external stretching force,  $\bar{P} = P/(\sigma_{eq,c}A)$ , during one loading-unloading cycle, where  $A = \pi r_0^2$  is the area of cross section and  $\Delta_{\text{end}}^c = \sigma_{eq,c}L/E$  is the maximum stretching displacement of rod in its elastic regime. When the structure is in the elastic domain, i.e.  $P \leq \sigma_{eq,c}A$ , the slope of loading process is 1; when the normalized stretching force exceeds 1, the material undergoes plastic deformation, such that the slope of the loading curve decreases to  $E_t/E = 0.5$ . The evolution of plastic domain during the loading process is in Fig. 2(c1). During the unloading process, the rate of the curves is 1, and the elastic strain recovers to zero when the external force is absent. On the other hand, because of the irreversible plastic strain, the end displacement is non-zero after one loading-unloading cycle. A good match between analytical result and numerical data indicates the correctness of our discrete model.

### 3.2. Bending of a simply supported beam

We next consider a simply supported beam under a concentrated force located at its midpoint, as shown in Fig. 2(a2). Here, we model a square cross section with side width  $w = 1\text{ mm}$  (cross section area  $A = 1\text{ mm}^2$ ); also, the Young's modulus is  $E = 100\text{ GPa}$ , and the tangent modulus  $E_t$  is set to be zero, such that the analytical solution can be easily obtained. Even though our discrete model can seamlessly handle the geometrically nonlinear deformation (a validation case in fully nonlinear geometry could be found in Appendix E), we want to remain in linear regime where analytical solution (described next) is valid. As such, we define the critical yield stress as  $\sigma_{eq,c} = 1\text{ MPa}$  and this results in a deflection that is always in linear regime ( $\sim 0.01L$ ). We discretize the rod centerline into  $N = 51$  nodes and  $M = 10 \times 10$  elements after a convergence study, details can be found in Appendix A.

The analytical solution of elasto-plastic Euler-Bernoulli beam is given by [19]

$$\frac{\Delta_{\text{max}}}{\Delta_{\text{max}}^c} = \begin{cases} \bar{P} & \bar{P} < 1 \\ \left(5 - (\bar{P} + 3)\sqrt{3 - 2\bar{P}}\right) / \bar{P}^2 & 1 < \bar{P} < \frac{3}{2}, \end{cases} \quad (13)$$

where  $\bar{P} = PwL/(8\sigma_{eq,c}I)$  is the normalized external force and  $\Delta_{\text{max}}^c = \sigma_c L^2/(6Ew)$  is the critical midpoint displacement when the beam transforms from pure elastic to elasto-plastic state.

In Fig. 2(b2), we display the normalized concentrated force,  $\bar{P}$ , as a function of the normalized maximum deflection,  $\Delta_{\text{max}}/\Delta_{\text{max}}^c$ , during one loading-unloading cycle. The external force first linearly increases as the deflection goes up; while a nonlinear phase moderately appears and the structure undergoes plastic deformation when the normalized concentrated force goes beyond the critical,  $\bar{P} \geq 1$ . Importantly, the transformation from elastic phase to elasto-plastic phase is not a sudden change discussed in previous uniaxial stretching case, because the non-uniformed stress distribution along beam cross section implies that the plastic

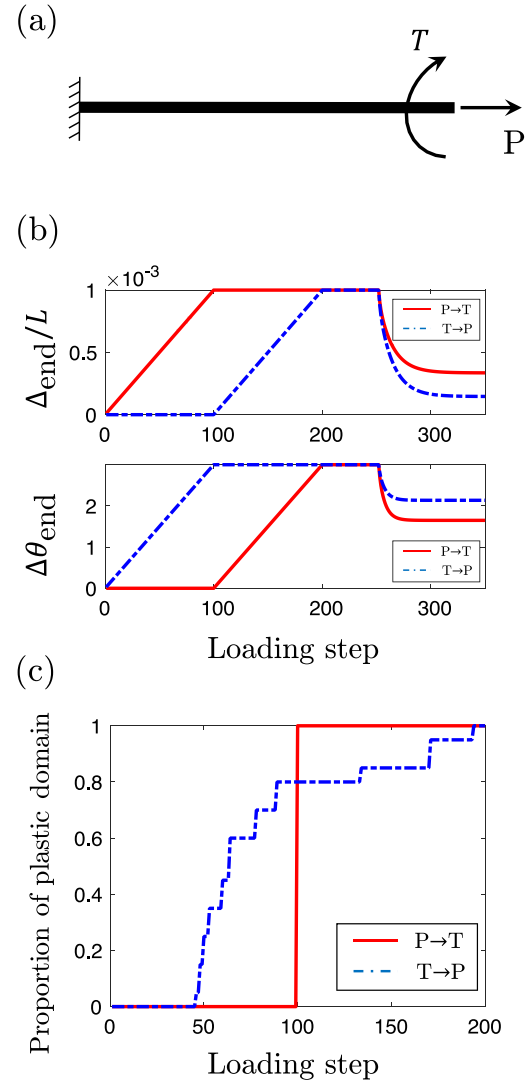


**Fig. 3.** (a) Diagram of the coupling between stretching and twisting of a rod. (b) Loading sequence as a function of time step number: solid line is stretching first ( $P \rightarrow T$ ), and dashed line is twisting first ( $T \rightarrow P$ ). (c) Portion of the plastic region during the loading process.

domain would gradually enlarge. The evolution of plastic domain at the beam midpoint during the loading process is in Fig. 2(c2). The unloading process, similarly, follows a linear elastic path, and the residual deflection is from the plastic strain. The plastic regime remains fixed during the unloading phase. Again, the agreement between analytical result and numerical data proves the accuracy of our newly introduced increment-based discrete elasto-plastic rod simulation.

### 3.3. Stretching and twisting coupling

In this section, we use our discrete model to reveal the fact that the elasto-plastic response in structure is path dependent. Fig. 3(a) shows a diagram of the stretching and twisting coupling of a rod. The geometric and physical parameters are exactly the same as the uniaxial pulling case, except the tangent modulus  $E_t$  is set to be zero here. Similarly, the rod is discretized into  $N = 20$  nodes and  $M = 80$  elements.

In Fig. 3(b), we display two cases: stretching first then twisting (red solid line), and twisting first then stretching (blue dashed line). Then Fig. 3(c) shows the proportion of the plastic domain



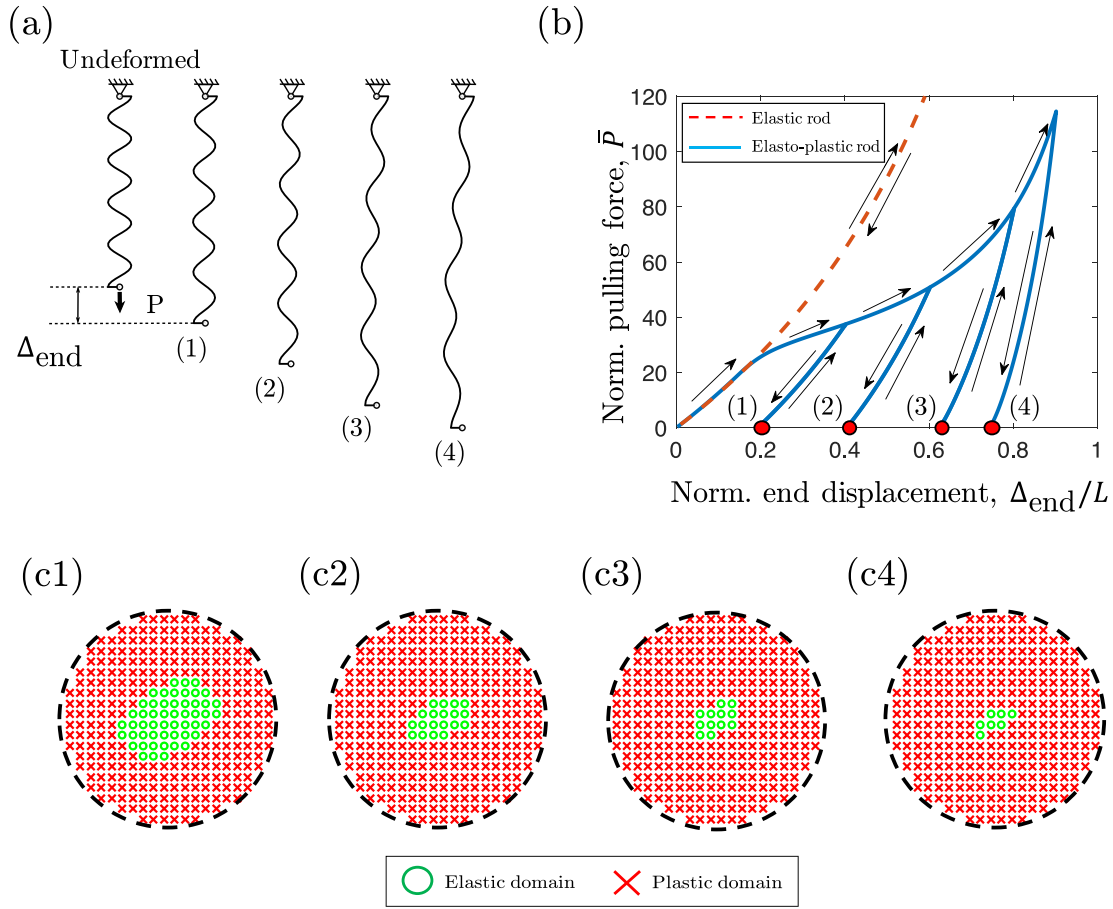


**Fig. 4.** (a) Configurations of a helical rod in stress-free and deformed conditions. (b) Normalized force-displacement curve during multiple loading-unloading loops. (c1)–(c4) The diagram of the development of plasticity area for a representative cross section during multiple loading-unloading loops.

for these two different cases during the loading process. The unloading process for these two cases are the same, i.e. we simultaneously release the stretching and torsion at the 250th loading step. Due to plastic strain, the rod would experience an irreversible deformation. The rods remain in different equilibrium configurations by changing the loading paths: the irreversible extension will be larger when stretching force is exerted first, compared with the case when torque is applied first. A qualitative explanation is as follows. The increment of plastic strain,  $d\epsilon_p$ , is always normal to the criterion stress surface and parallel to  $\partial f / \partial \sigma$  such that for the stretching first case, the major stress component is  $\sigma_{33}$  and  $d\epsilon_p$  will mainly go along the direction of  $\sigma_{33}$ .

### 3.4. Pulling of a helical rod

Finally, we consider a helical rod under an axial pulling force. We limited ourselves in geometrically linear regime for quantitative comparison between analytical results and numerical data in the previous demonstrations; here, we use a helical filament, referring to Fig. 4(a), to demonstrate that DEPR model can effectively capture both geometric nonlinearity and material nonlinearity. The geometric parameters are: circular cross section  $r_0 = 1.0$  mm, helical pitch  $\lambda_h = 22.0$  cm, helical radius  $R_h = 6.1$  cm, helical axis length  $L = 1.0$  m (resulting in a rod arclength  $s = 2.0$  m); the physical parameters are: Young's Modulus  $E = 100$  GPa, tangent modulus  $E_t = 0.1E$ , Poisson's ratio is  $\nu = 0.3$ , the critical stress  $\sigma_{eq,c} = 0.001E$ . We discretize the helical rod into  $N = 81$  nodes and  $M = 316$  elements at each vertex.

In Fig. 4(b), we quantify the normalized pulling force,  $\bar{P} = PL^2/(EI)$ , by measuring the normalized tip displacement,  $\Delta_{\text{end}}/L$ , during multiple loading-unloading loops (the path is illustrated by the arrows). The stretching force first slowly increases as the enlarge of the tip displacement, and a good match can be found between previous DER method and newly developed DEPR model in elastic regime. In the fully elastic case, the pulling force predicted by elastic model increases faster as the helical rod increases in axial length. On the other hand, the elasto-model shows that the rate of increase of pulling force (with end displacement), i.e. the slope of the curve in Fig. 4(b), decreases at  $\Delta_{\text{end}}/L \approx 0.2$  where the material starts to transition from elastic to elasto-plastic domain. Eventually, the pulling force measured by DEPR model also presents a rapidly increasing trend as a function of end displacement when the helical rod becomes more and more straight.

In addition, the configuration of the rod in unloaded state at four points during the loading-unloading process, marked by red dots in Fig. 4(b), are shown in Fig. 4(a). The elastic and plastic domains on the cross section at mid-point along the rod arc-length are illustrated in Fig. 4(c1)–(c4), from which we can clearly see the growth of the plastic domain. As the shape of elasto-plastic boundary for other nodes along rod arclength can be easily obtained by rotating the material frames to a certain angle, we only display a representative cross section for each state. The ellipse-like boundaries indicate the coupling between the twisting and bending when stretching a helical rod.

#### 4. Conclusion

We have developed a discrete numerical framework for the simulation of geometrically nonlinear deformation of one dimensional elasto-plastic structures. For this purpose, we first discretized the rod centerline into a number of nodes and edges, and formulated its geometrically nonlinear deformation following the well-established DER method. Next, the cross section of a rod at each node was meshed into multiple fiber-like elements, and the strain tensor at each fiber was related to the deformation of rod centerline. The stress tensor of each element, importantly, was then updated through a nonlinear increment-based return mapping algorithm during the time marching scheme; the internal forces, required to solving the equations of motion, were later numerically derived from the variation of strain energy. Several special cases – uniaxial stretching, bending of simply supported beam, stretching–twisting coupling, and pulling of a helical rod – were used to demonstrate the effectiveness and robustness of our newly introduced simulator. Moreover, the good agreements between analytical results and numerical data in some simple conditions indicated the correctness and accuracy of our numerical framework. We hope that the numerical tool can motivate further research in areas of computational plasticity as well as the design of plasticity-related advanced manufacturing processes, e.g. paper clip manufacturing.

#### Declaration of competing interest

The authors declare that they have no known competing financial interests or personal relationships that could have appeared to influence the work reported in this paper.

#### Acknowledgments

We acknowledge support from the National Science Foundation (Award # IIS-1925360) and the Henry Samueli School of Engineering and Applied Science, University of California, Los Angeles.

#### Appendix A. Discrete Elasto-Plastic Rods algorithm

In this section, we provide the pseudo code of Discrete Elasto-Plastic Rods method. At  $n$ th time step,  $t_n$ , we know the DOF vector  $\mathbf{q}_n$ , its velocity  $\mathbf{v}_n$ , and the stress and strain tensor of each element,  $\sigma_n^{(i,j)}$ ,  $\epsilon_n^{(i,j)}$ , where  $i \in [0, N-1]$ ,  $j \in [0, M-1]$ . Here  $N$  is the number of nodes and  $M$  is the element number on each vertex. We need to solve the equations of motion and update all the information from time  $t_n$  to time  $t_{n+1} = t_n + h$ . This time marching scheme is in Algorithm 1.

#### Appendix B. Gradient vector and Hessian matrix of strain energy

In this section, we provide a detailed formulation of the internal force vector in Eq. (8) (negative gradient of strain energy) as well as the Jacobian matrix in Eq. (12) (related to Hessian matrix of strain energy). First of all, we define the nabla operator  $\nabla$ ,

$$\nabla() = \mathbf{e}_m \frac{\partial}{\partial q_m} () \quad (\text{B.1a})$$

$$() \nabla = \frac{\partial}{\partial q_m} () \mathbf{e}_m \quad (\text{B.1b})$$

where we used Einstein notation (i.e. repeated indices imply summation over all values of the index),  $\mathbf{q} = q_m \mathbf{e}_m$  is the DOF of the system, and  $\mathbf{e}_m$  is a vector with zeros everywhere except at the  $m$ th position.

#### Algorithm 1 Discrete Elasto-Plastic Rods Algorithm

---

**Input:**  $tol, \mathbf{q}_n, \dot{\mathbf{q}}_n, \sigma_n^{(i,j)}, \epsilon_n^{(i,j)}$   
**Guess:**  $\mathbf{q}_{n+1}(0) \leftarrow \mathbf{q}_n + h\mathbf{v}_n$   
 $k \leftarrow 0$   
 $error \leftarrow 10 \times tol$   
**while**  $error > tol$  **do**  
 $\delta U \leftarrow 0$   
**for**  $i = 0$  to  $i = N - 1$  **do**  
**for**  $j = 0$  to  $j = M - 1$  **do**  
Calculate  $\epsilon_{n+1}^{(i,j)}(k)$  from Eq. (1), such that  $\delta \epsilon_{n+1}^{(i,j)}(k) = \epsilon_{n+1}^{(i,j)}(k) - \epsilon_n^{(i,j)}$   
Calculate  $\sigma_{n+1}^{(i,j)}(k) = \sigma_n^{(i,j)} + \delta \sigma_{n+1}^{(i,j)}(k)$  based on Algorithm 2  
 $\delta U \leftarrow \delta U + \sigma_{n+1}^{(i,j)}(k) : \delta \epsilon_{n+1}^{(i,j)}(k) \Delta S^{(i,j)} \Delta l_i$   
**end for**  
**end for**  
Compute  $\mathbf{F}_{n+1}^{int}(k)$  from Eq. (8)  
Compute  $\mathbf{E}_{n+1}(k)$  from Eq. (7a) and  $\mathbf{J}_{n+1}(k)$  from Eq. (12)  
 $\mathbf{q}_{n+1}(k+1) = \mathbf{q}_{n+1}(k) - \mathbf{J}_{n+1}(k) \backslash \mathbf{E}_{n+1}(k)$   
 $tol = \|\mathbf{E}_{n+1}(k)\|$   
 $k \leftarrow k + 1$   
**end while**  
 $\mathbf{q}_{n+1} = \mathbf{q}_{n+1}(k)$   
Update  $\mathbf{v}_{n+1}, \sigma_{n+1}^{(i,j)}, \epsilon_{n+1}^{(i,j)}$  from  $\mathbf{q}_{n+1}$   
**Output:**  $\mathbf{q}_{n+1}, \mathbf{v}_{n+1}, \sigma_{n+1}^{(i,j)}, \epsilon_{n+1}^{(i,j)}$

---

According to Eqs. (8) and (9b), the internal force vector is given by

$$\begin{aligned} \mathbf{F}_{n+1}^{int} &= -\frac{\partial U}{\partial \mathbf{q}} \\ &= -\sum_{i=0}^{N-1} \left\{ \sum_{j=0}^{M-1} [\sigma^{(i,j)} : (\epsilon^{(i,j)} \nabla)] \Delta S^{(i,j)} \right\} \Delta l_i, \end{aligned} \quad (\text{B.2})$$

where  $(\epsilon^{(i,j)} \nabla)$  is a geometry-related third-order tensor and can be expanded as

$$\begin{aligned} (\epsilon^{(i,j)} \nabla) &= \begin{bmatrix} 0 & 0 & -\frac{1}{2} Y^{(i,j)} \\ 0 & 0 & 0 \\ -\frac{1}{2} Y^{(i,j)} & 0 & 0 \end{bmatrix} (\tau_i \nabla) \\ &+ \begin{bmatrix} -\nu \frac{1}{2} X^{(i,j)} & 0 & 0 \\ 0 & -\nu \frac{1}{2} X^{(i,j)} & 0 \\ 0 & 0 & \frac{1}{2} X^{(i,j)} \end{bmatrix} (\kappa_i^2 \nabla) \\ &+ \begin{bmatrix} -\nu \frac{1}{2} Y^{(i,j)} & 0 & 0 \\ 0 & -\nu \frac{1}{2} Y^{(i,j)} & 0 \\ 0 & 0 & \frac{1}{2} Y^{(i,j)} \end{bmatrix} (\kappa_i^1 \nabla) \\ &+ \begin{bmatrix} -\nu & 0 & 0 \\ 0 & -\nu & 0 \\ 0 & 0 & 1 \end{bmatrix} (\epsilon_i^u \nabla). \end{aligned} \quad (\text{B.3})$$

The terms  $\tau_i \nabla$ ,  $\kappa_i^1 \nabla$ ,  $\kappa_i^2 \nabla$ , and  $\epsilon_i^u \nabla$  are gradients of the strain-related quantities with respect to the DOFs and can be found in standard DER method [38,40]. The size of these gradient vectors is  $4N - 1$  ( $N$  is the number of nodes) and only, at most, 11 elements (corresponding to three nodes and two edges) are non-zero. This significantly simplifies the programming implementation.

Eq. (B.2) for the internal force can now be re-written as

$$\begin{aligned} \mathbf{F}^{\text{int}} = & - \sum_{i=0}^{N-1} (\tau_i \nabla) \left\{ \sum_{j=0}^{M-1} \left[ \boldsymbol{\sigma}^{(i,j)} : \begin{bmatrix} 0 & 0 & -\frac{1}{2} Y^{(i,j)} \\ 0 & 0 & 0 \\ -\frac{1}{2} Y^{(i,j)} & 0 & 0 \end{bmatrix} \right] \right. \\ & \times \Delta S^{(i,j)} \left. \right\} \Delta l_i \\ & - \sum_{i=0}^{N-1} (\kappa_i^2 \nabla) \left\{ \sum_{j=0}^{M-1} \left[ \boldsymbol{\sigma}^{(i,j)} : \begin{bmatrix} -\nu \frac{1}{2} X^{(i,j)} & 0 & 0 \\ 0 & -\nu \frac{1}{2} X^{(i,j)} & 0 \\ 0 & 0 & \frac{1}{2} X^{(i,j)} \end{bmatrix} \right] \right. \\ & \times \Delta S^{(i,j)} \left. \right\} \Delta l_i \\ & - \sum_{i=0}^{N-1} (\kappa_i^1 \nabla) \left\{ \sum_{j=0}^{M-1} \left[ \boldsymbol{\sigma}^{(i,j)} : \begin{bmatrix} -\nu \frac{1}{2} Y^{(i,j)} & 0 & 0 \\ 0 & -\nu \frac{1}{2} Y^{(i,j)} & 0 \\ 0 & 0 & \frac{1}{2} Y^{(i,j)} \end{bmatrix} \right] \right. \\ & \times \Delta S^{(i,j)} \left. \right\} \Delta l_i \\ & - \sum_{i=0}^{N-1} (\epsilon_i^u \nabla) \left\{ \sum_{j=0}^{M-1} \left[ \boldsymbol{\sigma}^{(i,j)} : \begin{bmatrix} -\nu & 0 & 0 \\ 0 & -\nu & 0 \\ 0 & 0 & 1 \end{bmatrix} \right] \Delta S^{(i,j)} \right\} \Delta l_i, \end{aligned} \quad (\text{B.4})$$

where the first term on the right hand side is the twisting force, the second and third terms represent bending force, and the last term is the stretching force.

Similarly, the Hessian matrix of internal strain energy is

$$\begin{aligned} & \frac{\partial^2 U}{\partial \mathbf{q} \partial \mathbf{q}} \\ & = \sum_{i=0}^{N-1} \left\langle \sum_{j=0}^{M-1} \left\{ \nabla(\boldsymbol{\sigma}^{(i,j)}) : (\epsilon^{(i,j)} \nabla) + \boldsymbol{\sigma}^{(i,j)} : [(\epsilon^{(i,j)} \nabla) \nabla] \right\} \Delta S^{(i,j)} \right\rangle \Delta l_i \\ & = \sum_{i=0}^{N-1} \left\langle \sum_{j=0}^{M-1} \left\{ \left[ \nabla(\epsilon^{(i,j)}) : \frac{\partial \boldsymbol{\sigma}^{(i,j)}}{\partial \epsilon^{(i,j)}} \right] : (\epsilon^{(i,j)} \nabla) + \right. \right. \\ & \quad \left. \left. \boldsymbol{\sigma}^{(i,j)} : [(\epsilon^{(i,j)} \nabla) \nabla] \right\} \Delta S^{(i,j)} \right\rangle \Delta l_i, \end{aligned} \quad (\text{B.5})$$

where  $[(\epsilon^{(i,j)} \nabla) \nabla]$  can be expanded to write

$$\begin{aligned} [(\epsilon^{(i,j)} \nabla) \nabla] & = \begin{bmatrix} 0 & 0 & -\frac{1}{2} Y^{(i,j)} \\ 0 & 0 & 0 \\ -\frac{1}{2} Y^{(i,j)} & 0 & 0 \end{bmatrix} [(\tau_i \nabla) \nabla] \\ & + \begin{bmatrix} -\nu \frac{1}{2} X^{(i,j)} & 0 & 0 \\ 0 & -\nu \frac{1}{2} X^{(i,j)} & 0 \\ 0 & 0 & \frac{1}{2} X^{(i,j)} \end{bmatrix} [(\kappa_i^2 \nabla) \nabla] \\ & + \begin{bmatrix} -\nu \frac{1}{2} Y^{(i,j)} & 0 & 0 \\ 0 & -\nu \frac{1}{2} Y^{(i,j)} & 0 \\ 0 & 0 & \frac{1}{2} Y^{(i,j)} \end{bmatrix} [(\kappa_i^1 \nabla) \nabla] \\ & + \begin{bmatrix} -\nu & 0 & 0 \\ 0 & -\nu & 0 \\ 0 & 0 & 1 \end{bmatrix} [(\epsilon_i^u \nabla) \nabla], \end{aligned} \quad (\text{B.6})$$

and the terms  $[(\tau_i \nabla) \nabla]$ ,  $[(\kappa_i^1 \nabla) \nabla]$ ,  $[(\kappa_i^2 \nabla) \nabla]$ , and  $[(\epsilon_i^u \nabla) \nabla]$  are Hessians of the strain-related quantities with respect to the degrees of freedom [38,40]. Similar to the decomposition of the internal force into twisting, bending, and stretching terms in Eq. (B.4), the Hessian matrix can also be decomposed into four terms. For brevity, the details are not presented here. Importantly, when the element is in elastic domain, the term  $\frac{\partial \boldsymbol{\sigma}^{(i,j)}}{\partial \epsilon^{(i,j)}}$  is the elastic stiffness tensor  $\mathbb{D}$ . When plasticity occurs, on the other hand, the increment of stress tensor cannot be evaluated by analytical formulation and the general expression of  $\frac{\partial \boldsymbol{\sigma}^{(i,j)}}{\partial \epsilon^{(i,j)}}$  is unobtainable. Here, we assume that the gradient of the criterion function  $\frac{\partial f}{\partial \boldsymbol{\sigma}}$  is constant, such that the analytical formulation is given by,

$$\frac{\partial \boldsymbol{\sigma}}{\partial \boldsymbol{\epsilon}} = \mathbb{D} - \frac{(\mathbb{D} : \frac{\partial f}{\partial \boldsymbol{\sigma}}) (\frac{\partial f}{\partial \boldsymbol{\sigma}} : \mathbb{D})}{\frac{\partial f}{\partial \boldsymbol{\sigma}} : \mathbb{D} : \frac{\partial f}{\partial \boldsymbol{\sigma}} + H}, \quad (\text{B.7})$$

again, we ignore the superscript  $(i, j)$  for simplification. Note that the approximation of the Jacobian matrix only influences the convergence speed, while has no effect on the final solution.

### Appendix C. Implicit return-mapping algorithm

One of the important process in Algorithm 1 is to update the increment of stress tensor on the basis of the nonlinear constitutive law formulated in Eq. (11). For each element,  $(i, j)$ , we use  $\mathbb{R}_{n+1}$  to represent Eq. (11),

$$\mathbb{R}_{n+1} \equiv \begin{cases} f(\boldsymbol{\sigma}_{n+1}, \boldsymbol{\epsilon}_{p,n+1}) = 0 \\ \delta \boldsymbol{\sigma}_{n+1} - \mathbb{D} : [\delta \boldsymbol{\epsilon}_{n+1} - d\lambda_{n+1} \frac{\partial f(\boldsymbol{\sigma}_{n+1}, \boldsymbol{\epsilon}_{p,n+1})}{\partial \boldsymbol{\sigma}_{n+1}}] = 0, \end{cases} \quad (\text{C.1})$$

where  $\boldsymbol{\epsilon}_{p,n+1} = \boldsymbol{\epsilon}_{p,n} + \delta \boldsymbol{\epsilon}_{p,n+1}$ ,  $\boldsymbol{\sigma}_{n+1} = \boldsymbol{\sigma}_n + \delta \boldsymbol{\sigma}_{n+1}$ , and  $\mathbb{R}_{n+1}$  represents a total of 7 equations. Here, we ignore the superscript  $(i, j)$  for simplicity. Also, we use  $\mathbb{X}_{n+1}$  (vector of size 7) to represent the variables in these equations,

$$\mathbb{X}_{n+1} = \begin{bmatrix} d\lambda_{n+1} \\ \boldsymbol{\sigma}_{n+1} \end{bmatrix}, \quad (\text{C.2})$$

here, we re-write  $\boldsymbol{\sigma}_{n+1}$  as a vector of size 6. The Jacobian matrix is

$$\mathbb{J}_{n+1} = \begin{bmatrix} -H & \frac{\partial f_{n+1}}{\partial \boldsymbol{\sigma}_{n+1}} \\ \mathbb{D} : \frac{\partial f_{n+1}}{\partial \boldsymbol{\sigma}_{n+1}} & \mathbb{I} + d\lambda_{n+1} \left( \mathbb{D} : \frac{\partial^2 f_{n+1}}{\partial \boldsymbol{\sigma}_{n+1}^2} \right) \end{bmatrix}, \quad (\text{C.3})$$

where  $\mathbb{I}$  is the identity matrix in size of  $6 \times 6$ . Newton's iteration is used to update  $d\lambda_{n+1}$  as well as  $\boldsymbol{\sigma}_{n+1}$  by solving the 7 equations in Eq. (C.1), details are in Algorithm 2.

### Appendix D. Convergence study

In this appendix, we discuss the convergence of both node discretization and element discretization. We consider the simply supported beam of Fig. 2(a2) as a demonstration.

In Fig. D.5(a1), we plot the normalized external force,  $\bar{P}$ , as a function of normalized midpoint deflection,  $\Delta_{\text{max}}/\Delta_{\text{max}}^c$ , by varying the number of nodes,  $N \in \{5, 11, 31, 51\}$ . As  $N$  increases, the numerical result finally converges to the analytical solution. Here, we keep the number of elements along the cross-section  $M = 400$  fixed.

On the other hand, we use a similar plot, shown in Fig. D.5(a2), to show convergence with mesh number  $M$ . In this case, we keep  $N = 31$  fixed and switch the mesh number  $M \in \{25, 100, 400, 900\}$ . When the number of elements on each vertex is larger than 100, the final results will converge to analytical solution.



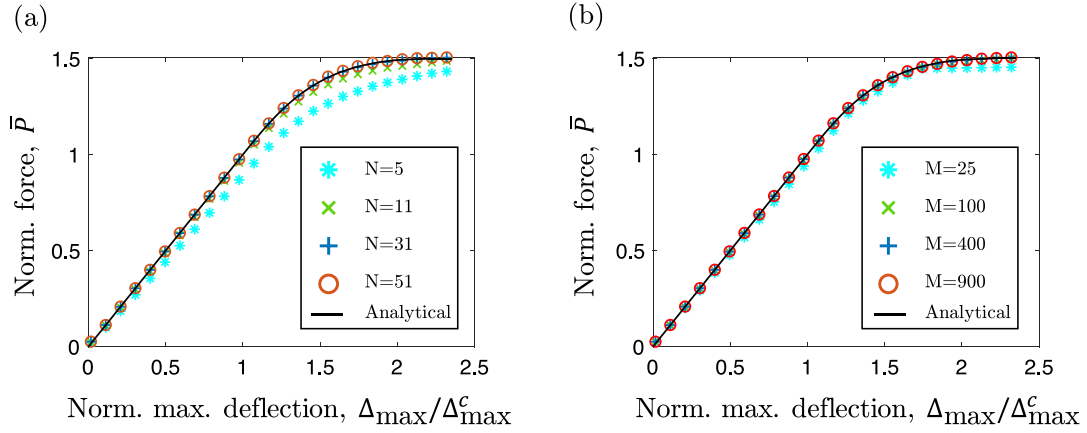


**Fig. D.5.** Normalized external force,  $\bar{P}$ , as a function of normalized midpoint deflection,  $\Delta_{\max}/\Delta_{\max}^c$ , by (a1) varying  $N \in \{5, 11, 31, 51\}$  and fixing  $M = 400$ ; and (a2) varying  $M \in \{25, 100, 400, 900\}$  and fixing  $N = 31$ .

#### Algorithm 2 Implicit Return-Mapping Method

**Input:**  $\text{tol}$ ,  $\epsilon_n$ ,  $\delta\epsilon_{n+1}$ ,  $\sigma_n$ ,  $\mathbb{D}$ , and  $H$   
**Guess:**  $\delta\sigma_{n+1}(0) = \mathbb{D} : \delta\epsilon_{n+1}$  and  $d\lambda_{n+1}(0) = 0$   
 Calculate  $f_{\text{elastic}} = f(\epsilon_n + \delta\epsilon_{n+1}, \sigma_n + \delta\sigma_{n+1}(0))$   
**if**  $f_{\text{elastic}} < 0$  **then**  
    $\delta\sigma_{n+1} = \delta\sigma_{n+1}(0)$   
**else**  
    $l \leftarrow 0$   
    $\text{error} \leftarrow 10 \times \text{tol}$   
   **while**  $\text{error} > \text{tol}$  **do**  
 Compute  $\mathbb{R}_{n+1}(l)$  and  $\mathbb{J}_{n+1}(l)$  from Eqs. (C.1) and (C.3)  
 $\mathbb{X}_{n+1}(l+1) = \mathbb{X}_{n+1}(l) - \mathbb{J}_{n+1}(l) \backslash \mathbb{R}_{n+1}(l)$   
 $\text{tol} = \|\mathbb{R}_{n+1}(l)\|$   
 $l \leftarrow l+1$   
   **end while**  
   Get  $\sigma_{n+1}$  from  $\mathbb{X}_{n+1}(l)$   
    $\delta\sigma_{n+1} = \sigma_{n+1} - \sigma_n$   
**end if**  
**Output:**  $\delta\sigma_{n+1}$

#### Appendix E. Comparison with finite element methods

In this appendix, we compare the DEPR framework with the Finite Element Method (FEM). We consider a simply supported beam in Fig. 2(a2). The width of the square cross section in this case is changed to 20 mm to reduce the number of elements in FEM. To demonstrate that DEPR method can handle the geometrically nonlinear regime, we choose the critical yield stress to be  $\sigma_{eq,c} = 2.5$  GPa, and the critical midpoint displacement when plastic state first occurs is  $\Delta_{\max}^c = 0.208$ . The maximum midpoint deflection is  $\Delta_{\max}/L \approx 0.3$ .

We use the commercial software Abaqus to run the FEM analysis. Both solid elements and beam elements are used in the FEM analysis. Considering the mechanics of pure bending, we simplified the model to a plane stress problem and used 5000 ( $10 \times 500$ ) four-node bilinear plane stress quadrilateral elements (Abaqus type CPS4). In addition, a FEM model using 100 two-node linear beam elements in space (Abaqus type B31) is also constructed.

In Fig. E.6, we plot the normalized external force,  $\bar{P}$ , as a function of normalized midpoint deflection,  $\Delta_{\max}/\Delta_{\max}^c$  from four different approaches: (i) FEM analysis with solid element, (ii) FEM analysis with beam elements, (iii) DEPR method, and (iv) analytical solution from Euler beam theory. The good match between

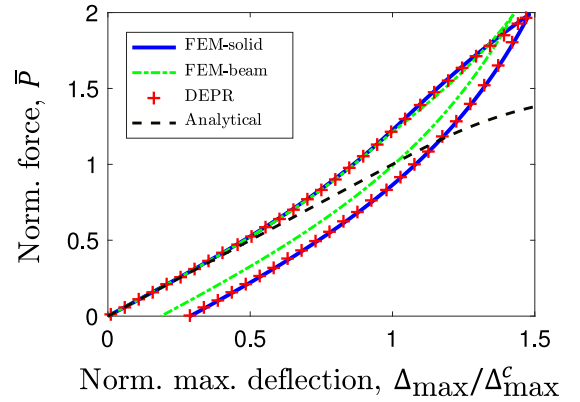


**Fig. E.6.** Normalized force-displacement curve in one loading-unloading cycle for simply supported beam using both FEM and DEPR method.

FEM analysis and DEPR method indicates the accuracy of our model in the geometrically nonlinear range.

#### Appendix F. Supplementary data

Supplementary material related to this article can be found online at <https://doi.org/10.1016/j.eml.2020.100767>.

#### References

- [1] E. Lauga, T.R. Powers, The hydrodynamics of swimming microorganisms, *Rep. Progr. Phys.* 72 (9) (2009) 096601.
- [2] S. Goyal, N.C. Perkins, C.L. Lee, Nonlinear dynamics and loop formation in kirchhoff rods with implications to the mechanics of dna and cables, *J. Comput. Phys.* 209 (1) (2005) 371–389.
- [3] P.M. Reis, H.M. Jaeger, M. Van Hecke, Designer matter: A perspective, *Extreme Mech. Lett.* 5 (2015) 25–29.
- [4] G. Kirchhoff, Über das gleichgewicht und die bewegung eines unendlich dünnen elastischen stabes, *J. Reine Angew. Math.* 56 (1859) 285–313.
- [5] M. Bergou, M. Wardetzky, S. Robinson, B. Audoly, E. Grinspun, Discrete elastic rods, *ACM Trans. Graph.* 27 (3) (2008) 63.
- [6] M. Gazzola, L. Dudte, A. McCormick, L. Mahadevan, Forward and inverse problems in the mechanics of soft filaments, *R. Soc. Open Sci.* 5 (6) (2018) 171628.
- [7] C. Lestringant, B. Audoly, D.M. Kochmann, A discrete, geometrically exact method for simulating nonlinear, elastic and inelastic beams, *Comput. Methods Appl. Mech. Engrg.* (2019) 112741.
- [8] B. Audoly, J.W. Hutchinson, One-dimensional modeling of necking in rate-dependent materials, *J. Mech. Phys. Solids* 123 (2019) 149–171.
- [9] J. Lubliner, *Plasticity Theory*, Courier Corporation, 2008.
- [10] U. Kocks, Realistic constitutive relations for metal plasticity, *Mater. Sci. Eng. A* 317 (1–2) (2001) 181–187.

- [11] W.F. Hosford, R.M. Caddell, *Metal Forming: Mechanics and Metallurgy*, Cambridge University Press, 2011.
- [12] W.-F. Chen, G.Y. Baladi, *Soil Plasticity: Theory and Implementation*, Vol. 38, Elsevier, 1985.
- [13] W.-F. Chen, *Plasticity in Reinforced Concrete*, J. Ross Publishing, 2007.
- [14] A. Ghaedizadeh, J. Shen, X. Ren, Y. Xie, Tuning the performance of metallic auxetic metamaterials by using buckling and plasticity, *Materials* 9 (1) (2016) 54.
- [15] M. Schenk, S.D. Guest, Geometry of miura-folded metamaterials, *Proc. Natl. Acad. Sci.* 110 (9) (2013) 3276–3281.
- [16] B. Ozbey, H. Demir, O. Kurc, V. Erturk, A. Altintas, Wireless measurement of elastic and plastic deformation by a metamaterial-based sensor, *Sensors* 14 (10) (2014) 19609–19621.
- [17] T. Henri-Édouard, *Mémoire sur l'écoulement des corps solides*, 1868.
- [18] T. Yu, W. Johnson, The plastica: the large elastic-plastic deflection of a strut, *Int. J. Non-linear Mech.* 17 (3) (1982) 195–209.
- [19] B. Štok, M. Halilović, Analytical solutions in elasto-plastic bending of beams with rectangular cross section, *Appl. Math. Model.* 33 (3) (2009) 1749–1760.
- [20] J.A. Kołodziej, P. Gorzelańczyk, Application of method of fundamental solutions for elasto-plastic torsion of prismatic rods, *Eng. Anal. Bound. Elem.* 36 (2) (2012) 81–86.
- [21] V. Sokolovsky, On a problem of elastic-plastic torsion, in: *Applied Mathematics Group*, Brown University, 1946.
- [22] J. Sokołowski, J. Zolesio, Sensitivity analysis of elastic-plastic torsion problem, in: *System Modelling and Optimization*, Springer, 1986, pp. 845–853.
- [23] G. Handelman, A variational principle for a state of combined plastic stress, *Quart. Appl. Math.* 1 (4) (1944) 351–353.
- [24] R. Hill, A variational principle of maximum plastic work in classical plasticity, *Quart. J. Mech. Appl. Math.* 1 (1) (1948) 18–28.
- [25] E. Imegwu, Combined plastic bending and torsion, *J. Mech. Phys. Solids* 10 (3) (1962) 277–282.
- [26] E. Imegwu, Plastic flexure and torsion, *J. Mech. Phys. Solids* 8 (2) (1960) 141–146.
- [27] F. Gaydon, H. Nuttali, On the combined bending and twisting of beams of various sections, *J. Mech. Phys. Solids* 6 (1) (1957) 17–26.
- [28] M. Steele, The plastic bending and twisting of square section members, *J. Mech. Phys. Solids* 3 (2) (1955) 156–166.
- [29] H. Ishikawa, Elasto-plastic stress analysis of prismatic bar under combined bending and torsion, *J. Appl. Math. Mech./Z. Angew. Math. Mech.* 53 (1) (1973) 17–30.
- [30] V. Kobelev, Elastic-plastic work-hardening deformation under combined bending and torsion and residual stresses in helical springs, *Int. J. Mater. Form.* 3 (2010) 869–881.
- [31] V. Kobelev, Elastoplastic stress analysis and residual stresses in cylindrical bar under combined bending and torsion, *J. Manuf. Sci. Eng.* 133 (4) (2011) 044502.
- [32] P.M. Miller, L.E. Malvern, Numerical analysis of combined bending and torsion of a work-hardening plastic square bar, *J. Appl. Mech.* 34 (4) (1967) 1005–1010.
- [33] J.C. Simo, T.J. Hughes, *Computational Inelasticity*, Vol. 7, Springer Science & Business Media, 2006.
- [34] G. Scalet, F. Auricchio, Computational methods for elastoplasticity: an overview of conventional and less-conventional approaches, *Arch. Comput. Methods Eng.* 25 (3) (2018) 545–589.
- [35] P. Wriggers, *Nonlinear Finite Element Methods*, Springer Science & Business Media, 2008.
- [36] D. Owen, E. Salonen, Three-dimensional elasto-plastic finite element analysis, *Internat. J. Numer. Methods Engrg.* 9 (1) (1975) 209–218.
- [37] E. Grinspun, M. Desbrun, K. Polthier, P. Schröder, A. Stern, *Discrete differential geometry: an applied introduction*, ACM SIGGRAPH Course 7 (2006) 1–139.
- [38] M. Bergou, B. Audoly, E. Vouga, M. Wardetzky, E. Grinspun, Discrete viscous threads, *ACM Trans. Graph.* 29 (4) (2010) 116.
- [39] B. Audoly, Y. Pomeau, *Elasticity and Geometry: From Hair Curls to the Non-Linear Response of Shells*, Oxford University Press, 2010.
- [40] M.K. Jawed, A. Novelia, O.M. O'Reilly, *A Primer on the Kinematics of Discrete Elastic Rods*, Springer, 2018.
- [41] X. Li, W. Huang, M.K. Jawed, A discrete differential geometry-based approach to numerical simulation of timoshenko beam, *Extreme Mech. Lett.* (2019) 100622.
- [42] Z. Shen, J. Huang, W. Chen, H. Bao, Geometrically exact simulation of inextensible ribbon, in: *Computer Graphics Forum*, Vol. 34, Wiley Online Library, 2015, pp. 145–154.
- [43] D. Baraff, A. Witkin, Large steps in cloth simulation, in: *Proceedings of the 25th Annual Conference on Computer Graphics and Interactive Techniques*, ACM, 1998, pp. 43–54.
- [44] E. Grinspun, A.N. Hirani, M. Desbrun, P. Schröder, Discrete shells, in: *Proceedings of the 2003 ACM SIGGRAPH/Eurographics Symposium on Computer Animation*, Eurographics Association, 2003, pp. 62–67.
- [45] C. Batty, A. Uribe, B. Audoly, E. Grinspun, Discrete viscous sheets, *ACM Trans. Graph.* 31 (4) (2012) 113.
- [46] C. Baek, A.O. Sageman-Furnas, M.K. Jawed, P.M. Reis, Form finding in elastic gridshells, *Proc. Natl. Acad. Sci.* 115 (1) (2018) 75–80.
- [47] M.L. Wilkins, *Calculation of Elastic-Plastic Flow*, Tech. rep., California Univ Livermore Radiation Lab, 1963.
- [48] R. Krieg, S. Key, Implementation of a time independent plasticity theory into structural computer programs, in: *Constitutive Equations in Viscoplasticity: Computational and Engineering Aspects*, 1976, pp. 125–137.
- [49] W. Huang, M.K. Jawed, Newmark-beta method in discrete elastic rods algorithm to avoid energy dissipation, *J. Appl. Mech.* 86 (8) (2019) 084501.